Journal of Geophysical Research: Space Physics

RESEARCH ARTICLE
10.1029/2018JA025819

Estimating the Kinetic Energy Budget of the Polar Wind Outflow

Kun Li[1], Y. Wei[1,2,3], S. Haaland[4,5], E. A. Kronberg[4,6], Z. J. Rong[1,2,3], L. Maes[4], R. Maggiolo[7], M. André[8], H. Nilsson[9], and E. Grigorenko[10]

[1]Chinese Academy of Sciences, Institute of Geology and Geophysics, Beijing, China, [2]College of Earth Science, University of Chinese Academy of Sciences, Beijing, China, [3]Chinese Academy of Sciences, Institutions of Earth Science, Beijing, China, [4]Max Planck Institute for Solar System Research, Göttingen, Germany, [5]Birkeland Centre for Space Science, Department of Physics and Technology, University of Bergen, Bergen, Norway, [6]Department of Earth and Environmental Sciences Geophysics, Ludwig Maximilian University of Munich, Munich, Germany, [7]Belgian Institute for Space Aeronomy, Brussels, Belgium, [8]Swedish Institute of Space Physics, Uppsala, Sweden, [9]Swedish Institute of Space Physics, Kiruna, Sweden, [10]Space Research Institute of RAS, Moscow, Russia

Key Points:
- Quantitative energy budget of the polar wind outflow has been estimated
- Solar wind energy input is the dominant energy source when the ε parameter is higher than 10^{10} W
- Solar illumination provides the kinetic energy of the polar wind outflow at a rate of about 10^{7} W, which is lower than the solar wind

Correspondence to:
K. Li,
li.kun@mail.iggcas.ac.cn

Citation:
Li, K., Wei, Y., Haaland, S., Kronberg, E. A., Rong, Z. J., Maes, L., et al. (2018). Estimating the kinetic energy budget of the polar wind outflow. *Journal of Geophysical Research: Space Physics*, *123*, 7917–7929. https://doi.org/10.1029/2018JA025819

Received 23 JUN 2018
Accepted 6 SEP 2018
Accepted article online 8 SEP 2018
Published online 22 SEP 2018

Abstract Ionospheric outflow from the polar cap through the polar wind plays an important role in the evolution of the atmosphere and magnetospheric dynamics. Both solar illumination and solar wind energy input are known to be energy sources of the polar wind. However, observational studies of the energy transfer from these two energy sources to the polar wind are difficult. Because of their low energy, polar wind ions are invisible to regular ion detectors onboard a positively charged spacecraft. Using a new technique that indirectly measures these low-energy ions, we are able to estimate the energy budget of the polar wind. Our results show that solar illumination provides about 10^{7} W of the kinetic energy of the polar wind, in addition to the energy transferred from the solar wind with a maximum rate of about 10^{8} W. The energy transfer efficiency of solar illumination to the kinetic energy of the polar wind is about 6 to 7 orders of magnitude lower than that of the solar wind. Moreover, daily and seasonal changes in the orientation of the geomagnetic dipole axis control solar illumination over the polar cap, modulating both energies of the polar wind and energy transfer efficiencies from the two energy sources.

1. Introduction

For the last few decades, ion outflow from the Earth's polar ionosphere has been recognized as an important source of ions in the magnetosphere. Many studies have shown that ion outflow plays an important role in ionosphere-magnetosphere coupling and magnetospheric dynamics (André & Cully, 2012; Chappell et al., 1987; Engwall, Eriksson, Cully, André, Puhl-Quinn, Vaith, & Torbert, 2009; Kronberg et al., 2014; Moore & Horwitz, 2007; Olsen, 1982; Welling et al., 2015; Yau et al., 2007). It is also believed that ionospheric outflow may have significantly affected the evolution of the atmosphere and thus the habitability of the Earth (Kulikov et al., 2007; Lundin et al., 2007; Wei et al., 2014).

A significant amount of ions escape from the Earth's polar cap ionosphere in the form of the polar wind (Axford, 1968; Banks & Holzer, 1968; Ganguli, 1996; Yau et al., 2007). These ions are accelerated by an ambipolar electric field due to the different scale heights between ions and electrons in the ionosphere. They escape from the polar cap ionosphere along the open field lines and flow into the magnetotail. Because of their ionospheric origin, the polar wind consists of cold ions with low kinetic and thermal energies (André et al., 2015; Engwall, Eriksson, Cully, André, Puhl-Quinn, Torbert, & Vaith, 2009; Li et al., 2012; Su et al., 1998).

Two energy sources are considered to drive the polar wind outflow.

One significant energy source for the polar wind outflow is the solar wind energy input into the magnetosphere. The energy dissipation in the polar ionosphere is enhanced by increasing solar wind energy input (Guo et al., 2012; Knipp et al., 2004). During periods with a southward interplanetary magnetic field (IMF), the solar wind energy enters the magnetosphere and enhances magnetospheric convection. This drives ionospheric convection over the polar cap and consequently increases energy dissipation in the ionosphere through collisions between ions and neutrals in the ionosphere (Körösmezey et al., 1992). Increased solar wind energy input can also trigger geomagnetic storms or substorms that are associated with enhanced particle precipitation and Joule heating in the polar ionosphere. Lu et al. (2016) found that on average 22–25% of the energy in the polar region (including particle precipitation and Joule heating) dissipates in

the polar cap during a geomagnetic storm. This energy dissipation may be attributed to an enhancement of the polar wind during periods of geomagnetic activity (Engwall, Eriksson, Cully, André, Puhl-Quinn, Vaith, & Tobert, 2009; Li et al., 2012, 2017).

The other significant energy source is solar illumination. The ionosphere is essentially formed by ionizations due to extreme ultraviolet (EUV), X-rays, and the shorter wavelengths of the solar spectrum. The ion density of the polar wind is controlled by the solar EUV radiation (André et al., 2015). Heating due to solar illumination increases the ambipolar electric field that enables the polar wind outflow. The dependence of the outflow on solar zenith angle (SZA) is seen in both simulations (Glocer et al., 2012, 2017) and observations (Abe et al., 2004; Kitamura et al., 2011; Maes et al., 2017; Su et al., 1998). Daily and seasonal changes in the geomagnetic dipole tilt angle modulate illumination over the source region of the polar wind and consequently modulate the polar wind.

The energy transfer efficiencies between these energy sources and the polar wind outflow can be used as a proxy to estimate the ability of the Earth's magnetosphere to prevent the ionosphere from losing ions to space. These energy transfer efficiencies may vary in response to changes in the solar wind, solar illumination, and geomagnetic field. The various conditions of solar wind and the geomagnetic dipole may correspond to the different conditions over the history of the solar system and may help us to understand the evolution of the Earth's atmosphere and atmospheric loss from a magnetized exoplanet.

However, a quantitative study of the energy transfer based on in situ observations in the magnetosphere is difficult. Because a spacecraft in a sunlit and tenuous plasma environment is positively charged as a result of the photoelectron effect, the cold ions of the polar wind (with low kinetic and low thermal energies) are invisible to the ion detectors onboard spacecraft because their energies are lower than the electric potential energy of the spacecraft (Moore et al., 1997). The parameters of the polar wind at high altitudes were not available until they were reported by Engwall, Eriksson, Cully, André, Tobert, and Vaith (2009), who used electric field measurements to derive data of the polar wind. André et al. (2015) extended the data to cover most parts of the solar cycle 23. These data have been used in several studies (e.g., Haaland et al., 2012, 2015; Li et al., 2012, 2013, 2017; Maes et al., 2017).

This study uses the data from André et al. (2015) to estimate the energy transfer from the two energy sources to the polar wind and to assess the energy budget of the polar wind. The results show that the energy budget changes with different solar wind conditions and tilt angles of geomagnetic dipole field. The results also give us a clue on how the polar wind outflow changes with the evolution of the solar wind and geomagnetic field. In section 2, we describe the data and method. Section 3 presents the results, which is followed by a discussion in section 4 and conclusions in section 5.

2. Methods

To study the modulation of the solar wind energy input and solar illumination on the polar wind outflow, we combined data sets of the solar wind and cold ions in the magnetosphere. They are described in the following sections.

2.1. Solar Wind Energy Input Rate

We use the ε parameter (Perreault & Akasofu, 1978) in the present study to estimate the solar wind energy input rate. It is calculated in terms of the Poynting flux that enters the magnetosphere. The energy entering is modulated by the IMF clock angle (θ), and the total input rate is related to the cross-sectional area of the magnetosphere. After it was introduced by Perreault and Akasofu (1978), several modifications have been proposed. To include the variation of the size of the magnetosphere due to changes in the solar wind dynamic pressure, several studies replaced the fixed effective cross-sectional area of the magnetosphere with the variable one as $R_{cf}^2 = \left(B_0/4\pi\rho V_{SW}^2\right)^{\frac{1}{3}} R_E^2$, where B_0~3 × 10^4 nT is a constant given by Mac-Mahon and Gonzalez (1997), ρ is the mass density of the solar wind, V_{SW} is the speed of the solar wind, and R_E is the Earth's radius. In the present study, the ε parameter is thus calculated as

$$\varepsilon = \frac{4\pi}{\mu_0} V_{SW} B^2 \sin^4\frac{\theta}{2} R_{cf}^2 \quad (1)$$

where μ_0 is the magnetic permeability and B is the magnitude of the IMF.

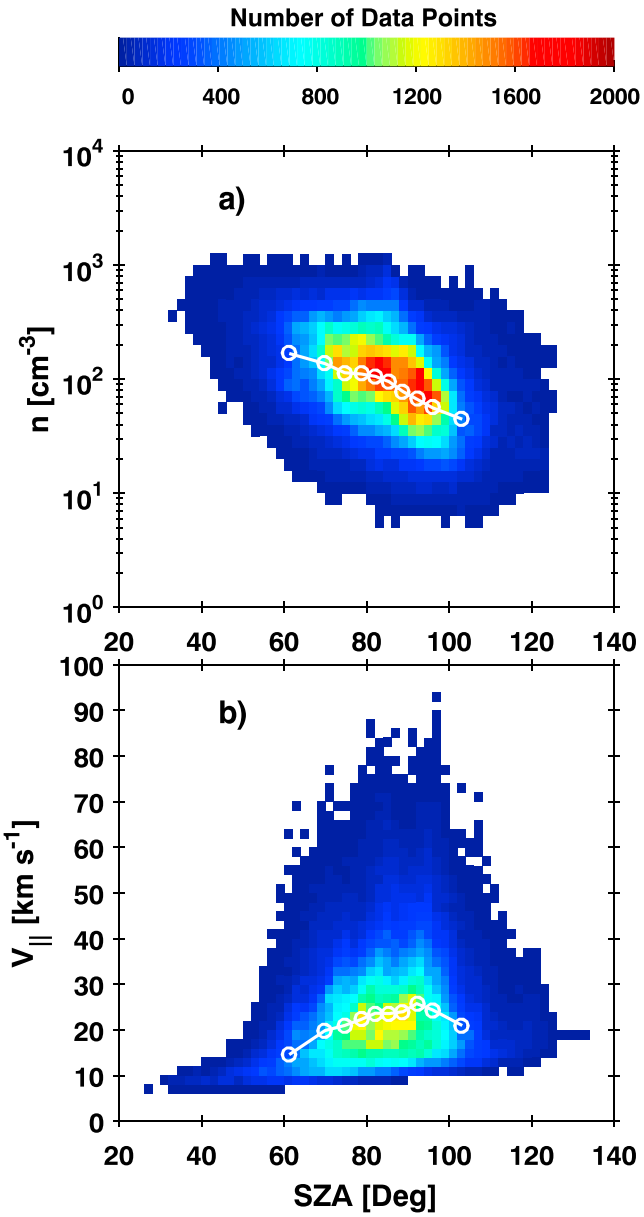

Figure 1. (a) Number of data points as a function of density at 1,000-km altitude (inferred from particle tracing) and solar zenith angle (SZA). (b) Number of data points as a function of outflow velocity at 1,000-km altitude (also inferred from particle tracing) and SZA. The white line with circles in each panel shows the median values of the parameter in the corresponding SZA ranges. The plotted median values include an equal fraction of all data points.

This ε parameter was also used by Li et al. (2017). The solar wind and the IMF parameters time shifted to the bow shock nose are obtained from the OMNI data set, with a 1-min resolution.

2.2. Estimating the Parameters of Cold Ion Outflow in the Topside Ionosphere

The velocity of cold ions in the lobes are obtained from the observations of plasma wake downstream of spacecraft. The derivation of cold ion velocities using the wake observation was first conducted by Engwall, Eriksson, Cully, André, Puhl-Quinn, Torbert, and Vaith (2009). Their data set contained about 176,000 measurements of cold ions in the lobes from 2001 to 2005. Later, André et al. (2015) extended the data set based on the same method. They used observations made by two Cluster spacecraft (C1 and C3) from July to November in each year from 2001 to 2010. The extended data set contains approximately 330,000 measurements of the bulk velocities of cold ions. This data set also includes the densities of cold ions, which are obtained from measurements of spacecraft electric potential by assuming the electric neutrality of plasma (Lybekk et al., 2012). With a given velocity, heavy ions (e.g., O^+) typically have an energy exceeding the spacecraft potential energy (Nilsson et al., 2010), so that they can easily penetrate the wake. Therefore, the wake observation is more sensitive to light ions (H^+ and He^+). The cold ion data set is considered to contain only the parameters of protons. Of these 330,000 measurements, about 320,000 are identified as tailward flows. For details of this data set, we refer to the paper by André et al. (2015).

To study the polar wind in the ionosphere, Li et al. (2017) conducted backward particle tracing using the cold ion parameters obtained in the lobes and using the solar wind parameters given in the data set mentioned above. We use the tracing results from Li et al. (2017), which considered the relevant accelerations and magnetospheric convections. The tracing results include positions in the topside ionosphere at 1,000-km altitude, travel times from the topside ionosphere to the spacecraft, outflow particle flux (F_{DP}), density (n), parallel velocity ($V_{||}$), and perpendicular velocity in the topside ionosphere. For the details of the particle tracing, we refer the paper by Li et al. (2017).

2.3. Outflow Parameters as Functions of the SZA

Solar illumination controls ion production and the ambipolar electric field that enables outflow. Thus, the polar wind outflow is modulated by the SZA. As can be seen in Figure 1a, the density decreases with increasing SZA. Figure 1b shows that there is also a dependence of outflow parallel velocity on SZA with maximum velocity at an SZA of around 90°. On the dayside with a small SZA, the inferred $V_{||}$ may be influenced by the velocity filter effect. In this case, the spacecraft in the lobes would measure more ions from the dayside with low $V_{||}$than from the nightside. This effect would result in a smaller $V_{||}$ in a location with a smaller SZA, as shown in Figure 1b. This effect on our results will be discussed in section 4.1. On the nightside, $V_{||}$ decreases with increasing SZA. This may be attributed to a small ambipolar electric field because of a weak solar illumination.

To estimate the hemispheric outflow rates of kinetic energy from one record for a given position in the polar cap ionosphere at a specific time, n and $V_{||}$ must be known at locations in the polar cap with various SZAs (The polar cap is the region in the ionosphere magnetically connected to the magnetotail; Siscoe & Huang, 1985). Here we use least square fitting to approximate n and $V_{||}$ as functions of SZA for a given solar EUV over various solar wind energy input ranges. We divide the data set into three groups according to the

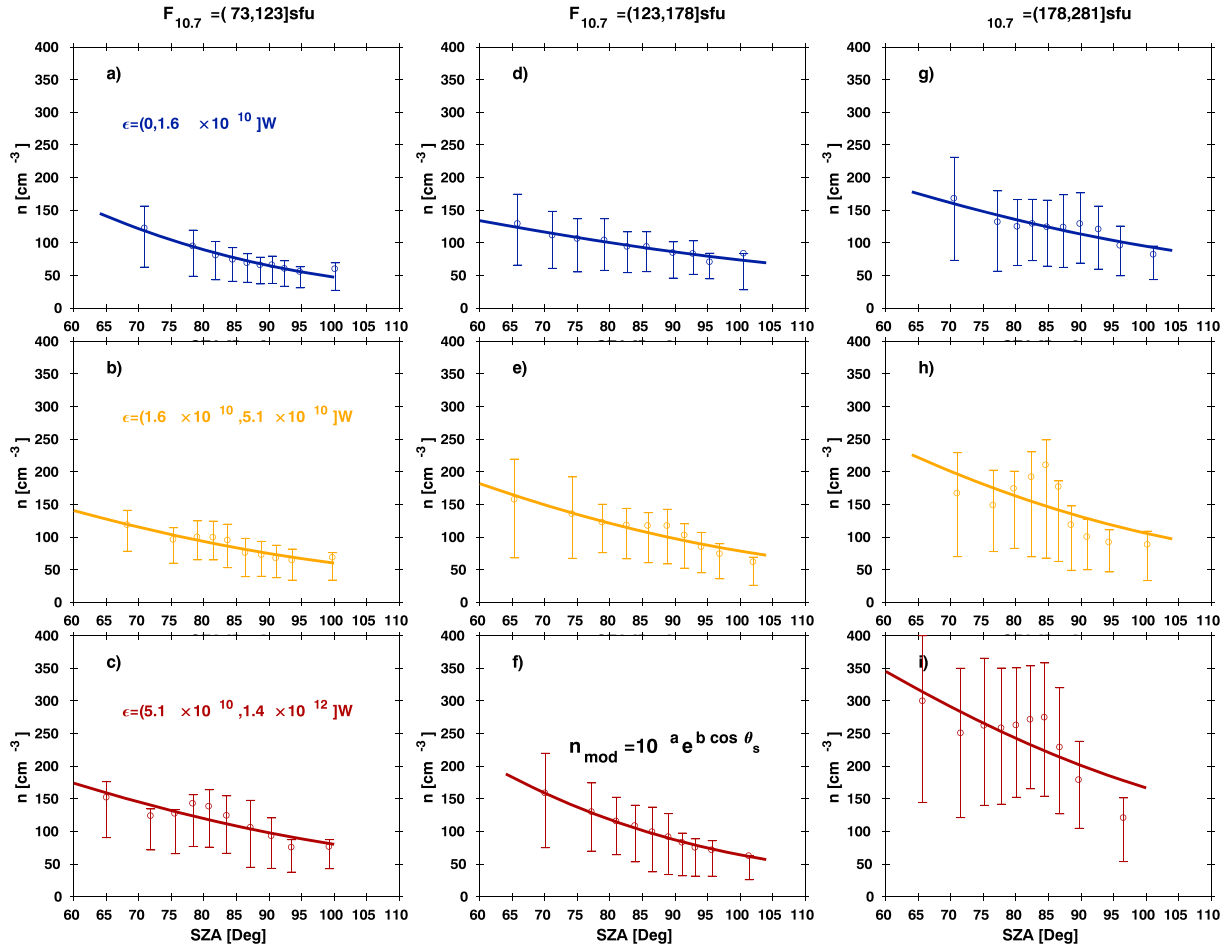

Figure 2. (a–i) The least square fitting and distributions of outflow density at 1,000-km altitude (n) as functions of solar zenith angle (SZA) for different ranges of $F_{10.7}$ index and the ε parameter. Each panel includes the data in the range of $F_{10.7}$ index indicated at the top of the column, and in the range of the ε parameter indicated by the legend in Figures 2a–2c. The ranges for each panel are set to include the optimal number of data points. The solid curve in each panel is the curve fitted with the data, following the equation shown in Figures 2f. The mean values of density in each SZA interval are shown as colored circles with error bars indicating the first and the third quartiles.

$F_{10.7}$ index and ε parameter with each group having the same number of data points. This results in a total of nine subsets of data.

Because the calculation of the hemispheric outflow rate of kinetic energy F_E contains only outflow from the polar cap, the data used for fitting to the empirical model and following statistics do not include ions originating from regions equatorward of the estimated polar cap. Most of these ions are derived to be from the dayside because of the high tailward ionospheric convection in these cases. For this reason, the original data points from particle tracing are reduced from approximately 237,000 (Li et al., 2017) to approximately 181,000.

Kitamura et al. (2011) studied the density of photoelectrons measured by Akebono spacecraft at various altitudes. They fitted photoelectron density as a function of altitude and SZA using an empirical model. In the present study, we assume overall the charge neutrality and simplified the model:

$$n_{\mathrm{mod}}(\theta_S) = 10^a e^{b\cos\theta_S} \tag{2}$$

where n_{mod} is the modeled density at 1,000-km altitude, θ_S is the SZA, and a and b are the coefficients to be determined. n_{mod} is shown as solid curves in Figure 2, with different ranges of the $F_{10.7}$ index (indicated on the top of each column). The different colors represent the different ranges of the ε parameter (indicated by

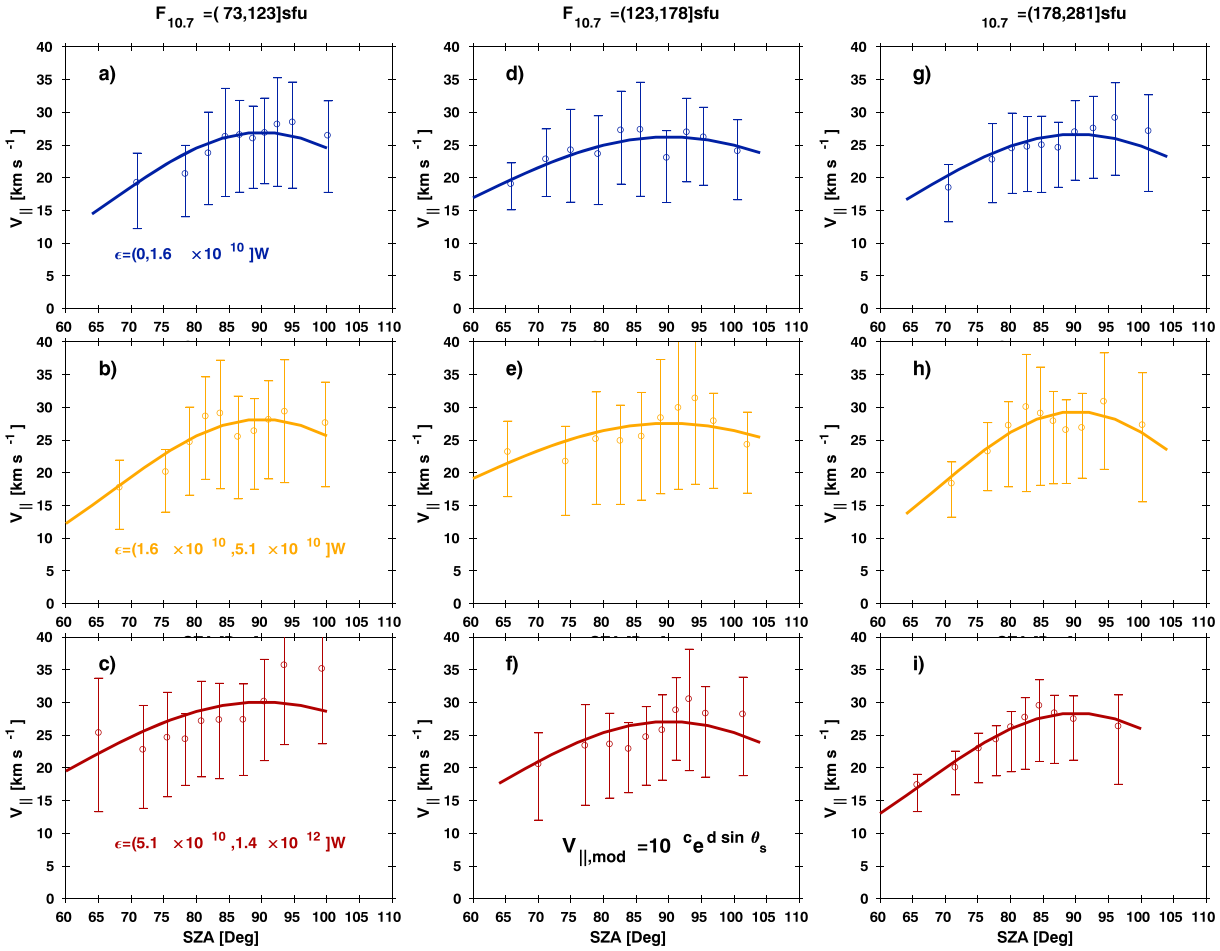

Figure 3. The least square fitting and distributions of outflow velocity at 1000 km altitude ($V_{||}$) as functions of solar zenith angle (SZA) for different ranges of $F_{10.7}$ index and the ε parameter, in the same format as Figure 2. The curve fitting follows the equation indicated in Figure 3f.

the legend in Figures 2a–2c). Mean values of n are shown as circles with error bars. SZA intervals are set to have the same number of data points. Error bars indicate the first and third quartiles in the SZA intervals.

It can be seen in Figure 2 that the actual values of n as a function of SZA change in almost the same pattern as the fitted curves. The magnitude of n determined by coefficient a increases with increasing $F_{10.7}$ index and ε parameter. To maintain the same patterns of the variation of n as functions of SZA for the following calculations, we use the coefficient b from the curve fitting but use a variable coefficient a determined from the actual density (n) inferred from particle tracing:

$$a = \log_{10} \frac{n}{e^{b \cos\theta_S}} \tag{3}$$

We slightly modify the curve fitting for $V_{||}$, following a similar empirical method:

$$V_{\parallel,\mathrm{mod}}(\theta_S) = 10^c e^{d \sin\theta_S} \tag{4}$$

where the coefficient d is determined from curve fitting, and the coefficient c is determined from

$$c = \log_{10} \frac{V_{\parallel}}{e^{d \sin\theta_S}} \tag{5}$$

Figure 3 shows the fitted $V_{||}$ as solid curves with the ranges of the $F_{10.7}$ index indicated at the top of each column and with the ranges of the ε parameter indicated in Figures 3a–3c. Mean values of $V_{||}$ are indicated as

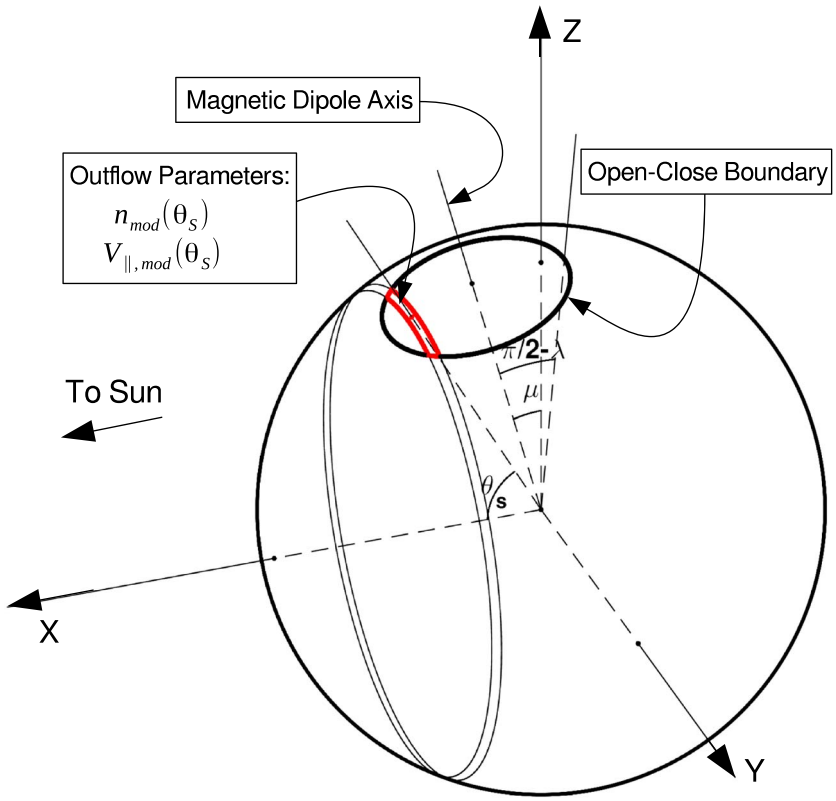

Figure 4. Geometry of the polar cap used for calculating the hemispheric outflow rate of kinetic energy and particles of the polar wind in the GSM system (see equation (6)). The Sun is to the left. The spherical area in the polar cap shown in red, with a solar zenith angle of θ_S, is bordered by the largest and smallest solar zenith angle in the interval of $\Delta\theta_S$ and the open-close boundary, where μ is the hemispheric magnetic dipole tilt angle and λ is the magnetic latitude of the open-close boundary. The λ is controlled by the interplanetary magnetic field and strength of the geomagnetic activity as illustrated in equation (7).

circles with error bars in the SZA intervals, in the same format as those for n. The modeled n and $V_{\parallel}$ are analog to most of the actual mean values. In the following, parameters with the subscript *mod* denote the parameters unavailable in the data from particle tracing and are instead estimated from the empirical model.

2.4. Estimating the Hemispheric Kinetic Energy Outflow Rate of the Polar Wind

Because our data set contains only protons with a mass of m_p, F_E can be calculated as

$$F_E = \sum_{\theta_S} F_{DE,\mathrm{mod}}(\theta_S)\Delta S(\theta_S,\lambda,\mu) = \frac{1}{2} m_p \sum_{\theta_S} n_{\mathrm{mod}}(\theta_S) V^3_{\parallel,\mathrm{mod}}(\theta_S)\Delta S(\theta_S,\lambda,\mu) \quad (6)$$

where $F_{DE,\mathrm{mod}}(\theta_S) = 1/2 m_p n_{\mathrm{mod}}(\theta_S) V^3_{\parallel,\mathrm{mod}}(\theta_S)$, $\Delta S(\theta_S,\lambda,\mu)$ is the area of the topside ionosphere at 1,000-km altitude, with an SZA of θ_S. This area is bordered by the largest and smallest SZA in the interval of $\Delta\theta_S$, and the magnetic open-close boundary with the magnetic latitude of λ (see the area bordered by red solid lines in Figure 4). The SZAs of the polar cap are also modulated by the hemispheric dipole tilt angle (μ) as shown in Figure 4.

Milan (2009) considered that the λ is controlled by the dayside reconnection rate (Φ_D) and the nightside merging rate estimated from the D_{st} index. They obtained the relationship between the λ, the Φ_D, and the D_{st} index by data fitting using approximately 40,000 images of the auroral oval from the Imager for Magnetopause-to-Aurora Global Explorer spacecraft. Their results have been used in the present study, with λ calculated as

$$\lambda = \frac{\pi}{2} - (18.2 - 0.038Dst + 0.042\Phi_D)$$
$$\Phi_D = 2.75 R_E V_{SW} \sqrt{B_y^2 + B_y^2} \sin^2\frac{\theta}{2} \quad (7)$$

where 2.75 R_E is a characteristic length scale and B_y and B_z are the y and z components of the IMF, respectively. The dipole tilt angle (μ) is estimated from the International Geomagnetic Reference Field 2011 model of the Earth's main magnetic field.

Because the outflow from the two hemispheres can differ from each other (Haaland et al., 2017), cold ion measurements in one hemisphere obtained from the spacecraft are considered to be inaccurate for the estimation of outflow fluxes and energies for both hemispheres. In the present study, F_E of one data point is calculated for the hemisphere where cold ion measurements are available.

3. Results

3.1. Energy Transferred From the Solar Wind

The control of the polar wind outflow by the solar wind energy input is demonstrated in Figure 5. Figure 5a shows the number of data points as a function of the ε parameter, indicating that the solar wind energy input rate estimated from the ε parameter in our data is mostly of the order of 10^{10} W. Figure 5b shows the hemispheric kinetic energy flux of the polar wind outflow (F_E) as a function of the ε parameter. The colored pixels indicate the number of data points in the corresponding ranges of F_E and ε. The white curve with circles indicates the median values of F_E. Each median value is calculated with the same number of data points. Figure 5c is the same as Figure 5b, but colored pixels now indicate the relative occurrence rate per bin of the ε parameter. The blue curve with circles is the median F_E and is the same as the one in Figure 5b. The brown curve with circles is the ratio between the median F_E and the ε parameter ($e_\varepsilon = F_E/\varepsilon$).

When the ε parameter increases from 10^{10} W to higher than 10^{11} W, the median F_E increases, as shown in Figures 5b and 5c. The ratio e_ε shown in Figure 5c is almost a constant of about 0.02% when the ε parameter is of the order of 10^{11} W. The linear relationship between the median F_E and the ε parameter of 10^{11} W indicates that F_E is mainly transferred from the solar wind energy input when the ε parameter is of the order of 10^{11} W.

From the curve of the median F_E, we see there is a transition in the ε parameter between 10^{10} and 10^{11} W in which the slope of the median F_E gradually became zero as the ε parameter decreases. This transition is caused by the relatively low rate of energy transfer from the solar wind.

When the ε parameter falls below 10^{10} W, F_E remains at around 10^7 W and e_ε increases linearly as the ε parameter decreases. This indicates that the rate of the energy transferred from the solar wind energy input is comparable to or lower than a rate of around 10^7 W, and the constant 10^7 W of the F_E is transferred from another energy source.

3.2. Energy Transferred From Solar Illumination

The energy transferred from sources other than the solar wind can be estimated when the solar wind energy input rate is extremely low. Figure 6 shows evidence that a large fraction of F_E is due to solar illumination when the ε parameter drops below 10^{10} W (marked by the red dashed vertical lines in Figures 6a and 6b). Figure 6a shows the relationship between the ε parameter and F_E for periods when more than 95% of the area of the polar cap is illuminated. The illuminated and dark areas are determined as $<90°$ and $>90°$ SZA, respectively. Figure 6b shows the same, but for periods when less than 95% of the area of the polar cap is illuminated. Curves with circles in Figures 6a and 6b show the median F_E, where each median value is calculated using the same number of data points.

Figure 6a indicates that the median F_E for almost the whole polar cap being illuminated is about 2×10^7 W, while the median F_E for almost the whole polar cap in the nightside is about 10^6 W, as shown in Figure 6b. The changes in solar illumination in the polar cap ionosphere led to a maximum change in the median F_E of about one order of magnitude. This large difference suggests that solar illumination provides energy to the polar wind outflow at a rate of the order of 10^7 W. The kinetic energy of the polar wind outflow from the nightside ionosphere is considered to partly originate from solar illumination as well. Indeed, ions with a long chemical

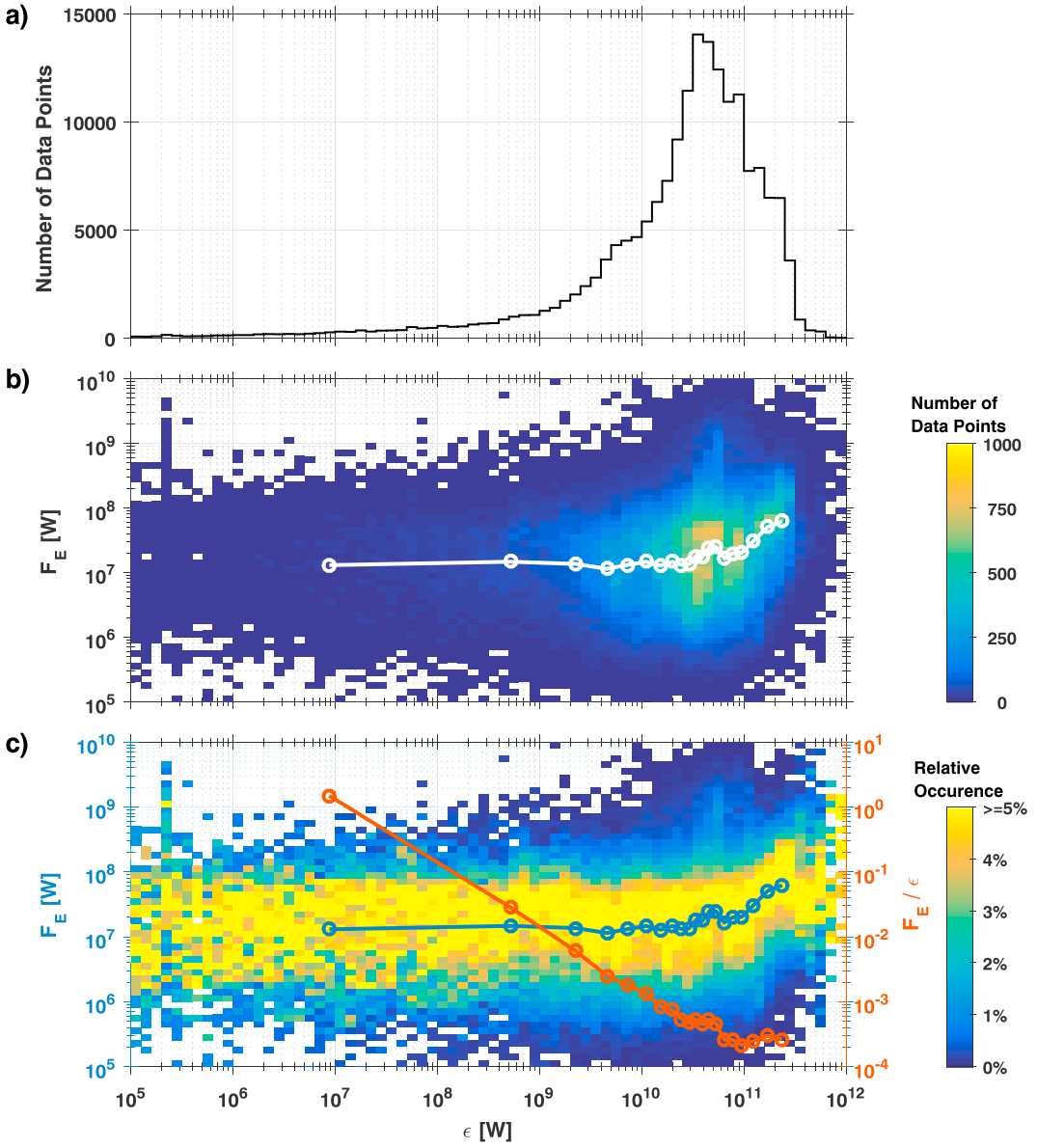

Figure 5. The polar wind outflow characteristics as a function of the ε parameter. (a) Distribution of the number of data points. (b) The hemispheric kinetic energy of the polar wind outflow (F_E). The colored pixels represent the numbers of data points in the given ranges of the F_E and ε parameter. The white circles show the median F_E, with each circle calculated using same number of data points. (c) The same as Figure 5b, but the colored pixels represent the relative occurrence rate per ε parameter. The blue circles are the same as the white ones in Figure 5b. The brown circles show the ratio between the median F_E and the median ε parameter. All three panels use the same *x* axis as shown at the bottom of Figure 5c.

lifetime are transported across the terminator from the dayside due to ionospheric convection, the rotation of the Earth, the circulation of the atmosphere, and plasma diffusion.

Figures 7a–7c show F_E, λ and the corresponding number of data points as functions of the percentage of illuminated area in the polar cap (q_{ill}). Each error bar in Figures 7a and 7b indicates the first quartile, median, and third quartile. Only data with $\varepsilon < 10^{10}$ W are included in these figures. Figure 7a suggests the median F_E gradually increases by about 1 order of magnitude as q_{ill} increased from 0% to 20%, while Figure 7b indicates that there is no simultaneous change in λ. This is considered reasonable because $\varepsilon < 10^{10}$ W often corresponds to a geomagnetic quiet time. Figure 7b suggests the increase in F_E is not caused by an enlargement of the polar cap. Judging from equation (6), it can be concluded that the increase in F_E is caused by increases

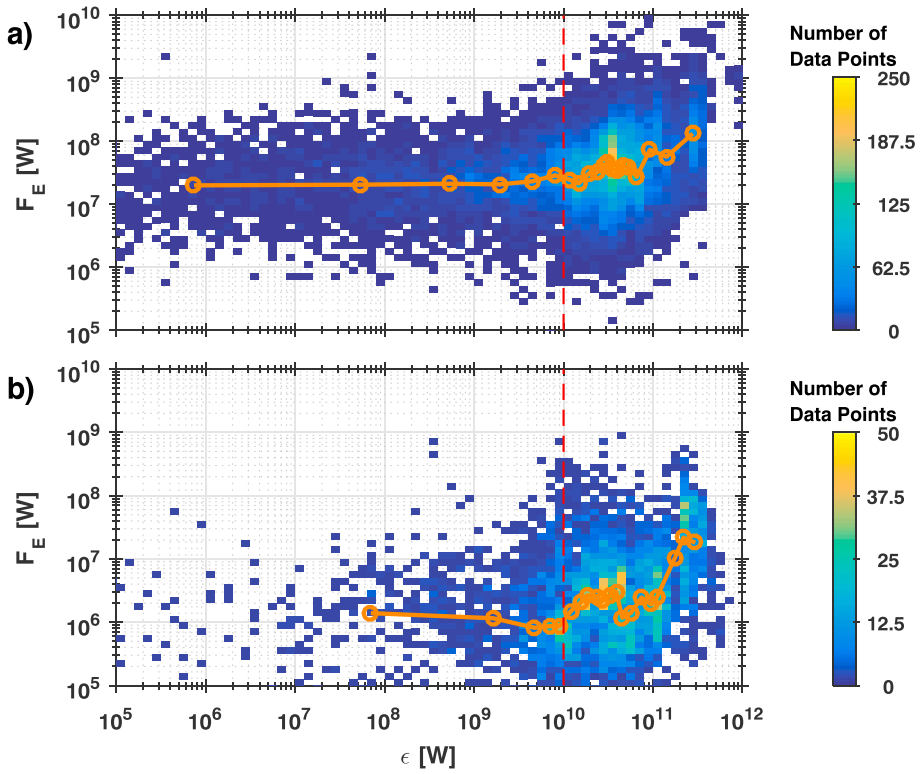

Figure 6. The modulation of the polar wind outflow by solar illumination. The F_E as a function of the ε parameter for the conditions when more than 95% of the area of the polar cap are (a) illuminated and (b) unilluminated. The brown circles in both panels are the median value of the F_E. The red dashed lines mark the ε parameters of 10^{10} W, below which the F_E does not systematically change with the value of the ε parameters. The difference in solar illumination caused one order of magnitude change in the median F_E for $\varepsilon < 10^{10}$ W.

in the F_{DE} and thus overall $F_{DE,\mathrm{mod}}$. Figure 7c indicates that the number of data points for q_{ill} intervals are comparable to each other and are therefore suitable for use in the above analysis. Therefore, with the significant difference in solar illumination between Figures 6a and 6b, we conclude that solar illumination is the main energy source of the polar wind outflow when the solar wind energy input rate is low.

It is worthy to note that the solar EUV of the illumination is the main driver of ion production. Due to changes in the geomagnetic dipole axis during a rotation or a revolution period, solar EUV irradiation over the polar cap changes more significantly than the variation of solar EUV emission during the solar cycle. Changing the geomagnetic dipole tilt angle has an effect of modulating the EUV irradiation over the polar cap and the polar wind outflow.

4. Discussion

4.1. Influence of the Velocity Filter Effect

As mentioned in section 2.3, $V_{||}$ in our data is affected by the velocity filter effect. Figure 1 suggests that the dependence of $V_{||}$on SZA is different from that of n. On the dayside, the median $V_{||}$ decreased with decreasing SZA. This effect resulted in a smaller $V_{||}$ in locations with a smaller SZA, as shown in Figure 1b. In addition, outflow from the dayside with very high parallel velocities may enter the magnetosheath or the mantle. This part of the outflow is therefore likely missed by the Cluster spacecraft and is not included in our dataset. Therefore, F_E in the present study may be underestimated.

Previous studies without the velocity filter effect suggest comparable outflow velocities between the dayside and the nightside. The simulation studies by Glocer et al. (2012, 2017) suggest that there is no significant day-night asymmetry in H^+ velocity at 1,000-km altitude, although a day-night asymmetry in the simulated H^+ density exists at the same altitude. Using measurements from POLAR spacecraft at 5,000-km altitude, Su

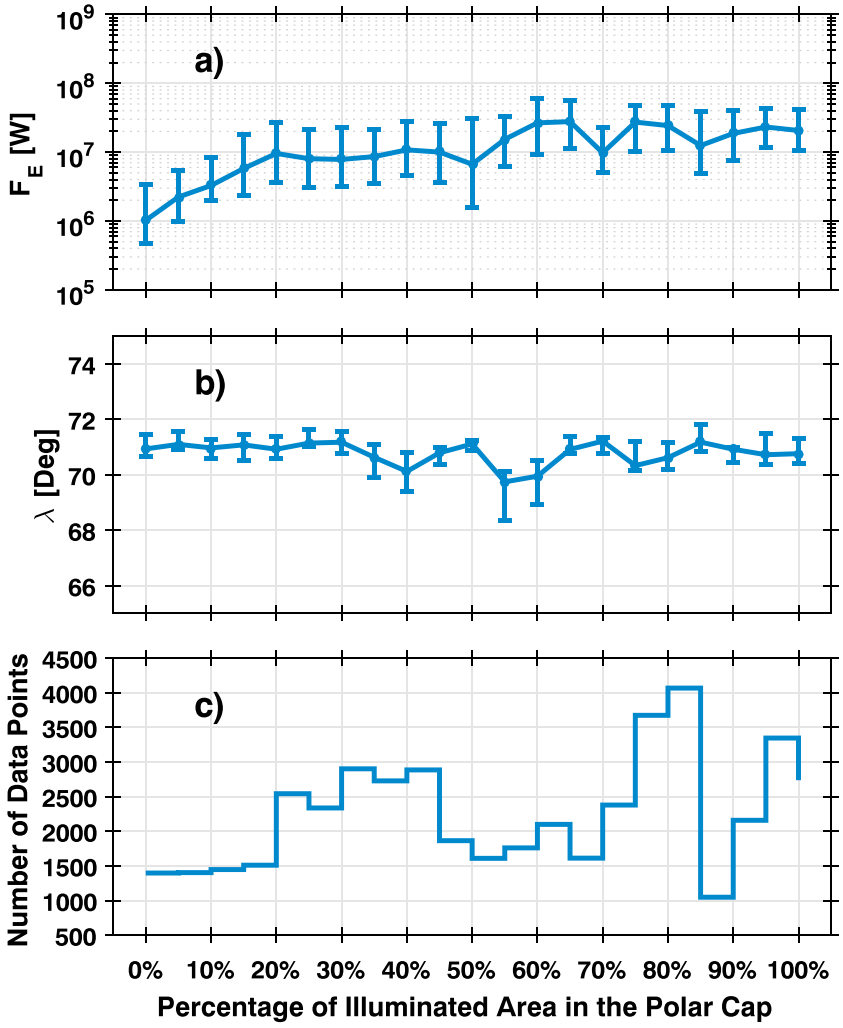

Figure 7. (a) F_E, (b) λ, and (c) number of data points as a function of percentage of illuminated area in the polar cap with interval of 5%. Only the data with $\varepsilon < 10^{10}$ W are shown here. Each error bar in Figures 7a and 6b indicates values of the first quartile, mean and the third quartile, respectively, from bottom to top.

et al. (1998) found no obvious dependence of H^+ velocity on SZA on the dayside, although they were not able to include measurements from the nightside.

To assess the influence of the velocity filter effect on our results, we modified the model illustrated in section 2.3 to exclude the velocity filter effect. We set the ratio of n on the dayside to the nightside as 2 at a given time. Based on the fact described in the previous paragraph, $V_{||}$ is set to be equivalent to any SZA in the polar cap at the same time. The dayside and nightside are separated by the boundary of the 90° SZA. Figure 8 shows the difference between the modified hemispheric outflow rate of kinetic energy of the polar wind (F_{EM}) and the F_E described in section 2. It can be seen that there are few cases with large differences between F_{EM} and F_E. As a consequence, these differences did not change our conclusions. Therefore, we assess that the influence of the velocity filter effect on our results is negligible.

4.2. Energy Transfer Efficiency Between the Outflow and Solar Illumination

Solar irradiance provides both energies and free ions to the polar wind outflow. Solar EUV emission causes ionization, while the solar radiation spectra with lower frequencies is responsible for the thermal irradiation over the ionosphere. The thermal irradiation affects the pressure gradient and the ambipolar electric field that drives the polar wind.

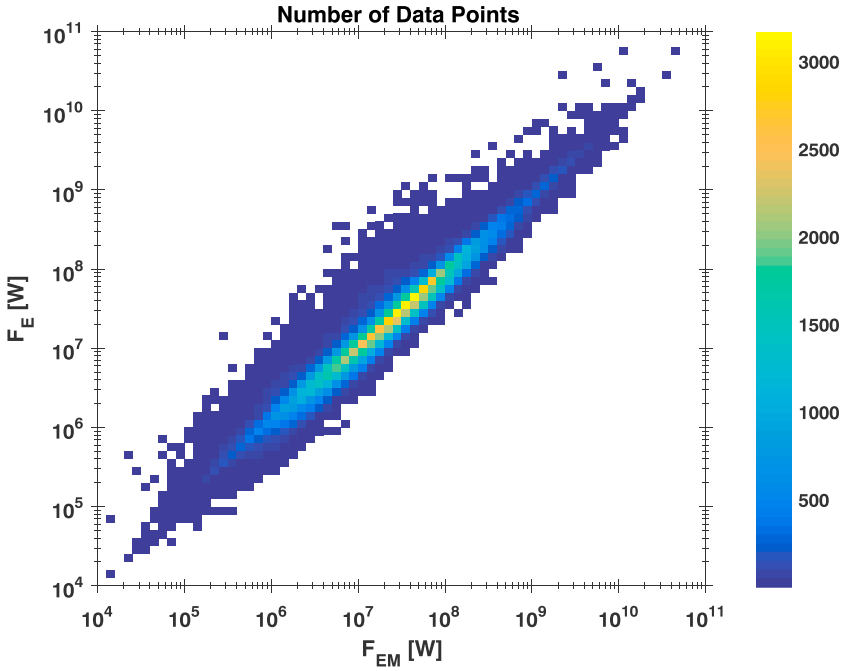

Figure 8. Comparison of the F_E described in section 2 to the F_{EM} that is modified from F_E to exclude the velocity filter effect. The details of F_{EM} are described in section 4.1.

We estimated the total energy power entering the ionosphere as a result of solar electromagnetic irradiation (E_T) as $E_T = TSI \cdot A = 2.32 \times 10^{17}$ W. The total solar irradiance (TSI) is a measure of solar electromagnetic irradiation over all wavelengths per unit area perpendicular to the sunlight and is measured as TSI = 1,361 W/m^2 (Kopp & Lean, 2010). A is the cross-sectional area of the topside ionosphere (1,000-km altitude) projected on the YZ plane of the geocentric solar ecliptic coordinate system.

Due to the rotation of the Earth and circulation of the atmosphere, part of the energy of the polar wind outflow may come from illumination at low latitudes. Likewise, the energy of ion outflow from the dark polar cap may originate from illumination on the dayside because ions with a long chemical lifetime may be transported across the terminator. Here we used the power of solar illumination over the illuminated ionosphere, E_T, to estimate the energy transfer efficiency between solar illumination and the F_E. Under the condition that more than 95% of the polar cap is illuminated (Figure 6a), the maximum energy transfer efficiency of solar illumination is estimated to be of the order of 10^{-10} (2×10^7 W/E_T). Meanwhile, the maximum transfer rate of energy from solar wind is about 10^8 W ($1.1 \times 10^8 - 2 \times 10^7$ W), and thus, energy transfer efficiency of the solar wind is about 3×10^{-4} ($10^8/3\times10^{11}$ W). Therefore, the energy transfer efficiency of solar illumination is approximately 6–7 orders of magnitude smaller than the transfer efficiency of the solar wind. Solar illumination is known to be one of the main drivers of the ion outflows from Mars and Venus at similar distances from the Sun but without a dipole magnetic field. The transfer efficiency can be used to compare the Earth with other planets to understand the ability of the Earth's magnetosphere to prevent the atmosphere from being lost into space.

5. Summary and Conclusion

In this study, we use particle tracing results to estimate the kinetic energy budget of the polar wind outflow in the topside ionosphere. We focus on the energy transfer between the two main energy sources and the polar wind outflow. Our results are summarized below.

When the ε parameter for estimating the solar wind energy input rate is of the order of 10^{11} W, an almost linear relationship between the hemispheric kinetic energy flux of the polar wind outflow, F_E, and the ε parameter suggests that the solar wind is the main energy source for the kinetic energy of the polar wind. The

median value of the F_E reaches 10^8 W for the maximum solar wind energy input rate in our data. As the ε parameter decreases to values between 10^{10} and 10^{11} W, F_E becomes less related to the solar wind energy input.

F_E remains constant when the ε parameter drops to below 10^{10} W, indicating that the solar wind energy input is not the main energy source for the outflow at this level. For a polar cap with more than 95% of area being illuminated, the median F_E is of the order of 10^7 W, while the median F_E for a polar cap with less than 5% of area being illuminated is about 1 order of magnitude lower at around 10^6 W. The difference in the F_E at different solar illuminations indicates that solar illumination is the main energy source when the solar wind energy input rate is extremely low. We estimate that the solar illumination transfers energy to the kinetic energy of the polar wind outflow at a rate of approximately 10^7 W.

Acknowledgments
This work is supported by the State Key Laboratory of Space Weather, Chinese Academy of Science, under Grant 2017-47F-01-04. This work is also supported by the National Natural Science Foundation of China (Grants 41704164, 41525016, 41474155, 41661164034, and 41621004). The low-energy ion data are based on the Cluster measurements available from the Cluster Science Archive (https://cosmos.esa.int/web/csa). Data selection, qualifying, and more details are described by André et al. (2015). The OMNI data of solar wind parameters is available from https://omniweb.gsfc.nasa.gov/form/omni_min.html.

References

Abe, T., Yau, A. W., Watanabe, S., Yamada, M., & Sagawa, E. (2004). Long-term variation of the polar wind velocity and its implication for the ion acceleration process: Akebono/suprathermal ion mass spectrometer observations. *Journal of Geophysical Research*, A09305. https://doi.org/10.1029/2003JA010223

André, M., & Cully, C. M. (2012). Low-energy ions: A previously hidden solar system particle population. *Geophysical Research Letters*, *39*, L03101. https://doi.org/10.1029/2011GL050242

André, M., Li, K., & Eriksson, A. I. (2015). Outflow of low-energy ions and the solar cycle. *Journal of Geophysical Research: Space Physics*, *120*, 1072–1085. https://doi.org/10.1002/2014JA020714

Axford, W. I. (1968). The polar wind and the terrestrial helium budget. *Journal of Geophysical Research*, *73*, 6855–6859. https://doi.org/10.1029/JA073i021p06855

Banks, P. M., & Holzer, T. E. (1968). The polar wind. *Journal of Geophysical Research*, *73*, 6846–6854. https://doi.org/10.1029/JA073i021p06846

Chappell, C. R., Moore, T. E., & Waite, J. H. J. (1987). The ionosphere as a fully adequate source of plasma for the Earth's magnetosphere. *Journal of Geophysical Research*, *92*, 5896–5910. https://doi.org/10.1029/JA092iA06p05896

Engwall, E., Eriksson, A. I., Cully, C. M., André, M., Puhl-Quinn, P. A., Torbert, R., & Vaith, H. (2009). Earth's ionospheric outflow dominated by hidden cold plasma. *Nature Geoscience*, *2*(1), 24–27. https://doi.org/10.1038/NGEO387

Engwall, E., Eriksson, A. I., Cully, C. M., André, M., Puhl-Quinn, P. A., Vaith, H., & Torbert, R. (2009). Survey of cold ionospheric outflows in the magnetotail. *Annales de Geophysique*, *27*(8), 3185–3201. https://doi.org/10.5194/angeo-27-3185-2009

Ganguli, S. B. (1996). The polar wind. *Reviews of Geophysics*, *34*, 311–348. https://doi.org/10.1029/96RG00497

Glocer, A., Khazanov, G., & Liemohn, M. (2017). Photoelectrons in the quiet polar wind. *Journal of Geophysical Research: Space Physics*, *122*, 6708–6726. https://doi.org/10.1002/2017JA024177

Glocer, A., Kitamura, N., Toth, G., & Gombosi, T. (2012). Modeling solar zenith angle effects on the polar wind. *Journal of Geophysical Research*, *117*, A04318. https://doi.org/10.1029/2011JA017136

Guo, J., Feng, X., Emery, B. A., & Wang, Y. (2012). Efficiency of solar wind energy coupling to the ionosphere. *Journal of Geophysical Research*, *117*, A07303. https://doi.org/10.1029/2012JA017627

Haaland, S., Eriksson, A., André, M., Maes, L., Baddeley, L., Barakat, A., et al. (2015). Estimation of cold plasma outflow during geomagnetic storms. *Journal of Geophysical Research: Space Physics*, *120*, 10,622–10,639. https://doi.org/10.1002/2015JA021810

Haaland, S., Eriksson, A., Engwall, E., Lybekk, B., Nilsson, H., & Pedersen, A. (2012). Estimating the capture and loss of cold plasma from ionospheric outflow. *Journal of Geophysical Research*, *117*, A07311. https://doi.org/10.1029/2012JA017679

Haaland, S., Lybekk, B., Maes, L., Laundal, K., Pedersen, A., Tenfjord, P., et al. (2017). North-south asymmetries in cold plasma density in the magnetotail lobes: Cluster observations. *Journal of Geophysical Research: Space Physics*, *122*, 136–149. https://doi.org/10.1002/2016JA023404

Kitamura, N., Ogawa, Y., Nishimura, Y., Terada, N., Ono, T., Shinbori, A., et al. (2011). Solar zenith angle dependence of plasma density and temperature in the polar cap ionosphere and low-altitude magnetosphere during geomagnetically quiet periods at solar maximum. *Journal of Geophysical Research*, *116*, A08227. https://doi.org/10.1029/2011JA016631

Knipp, D. J., Tobiska, W. K., & Emery, B. A. (2004). Direct and indirect thermospheric heating sources for solar cycles 21–23. *Solar Physics*, *224*(1-2), 495–505. https://doi.org/10.1007/s11207-005-6393-4

Kopp, G., & Lean, J. L. (2010). A new, lower value of total solar irradiance: Evidence and climate significance. *Geophysical Research Letters*, *38*, L01706. https://doi.org/10.1029/2010GL045777

Körösmezey, A., Rasmussen, C. E., Gombosi, T. L., & Khazaonv, G. V. (1992). Anisotropic ion heating and parallel O+ acceleration in regions of rapid E × B convection. *Geophysical Research Letters*, *19*, 2289–2292. https://doi.org/10.1029/92GL02489

Kronberg, E. A., Ashour-Abdalla, M., Dandouras, I., Delcourt, D. C., Grigorenko, E. E., Kistler, L. M., et al. (2014). Circulation of heavy ions and their dynamical effects in the magnetosphere: Recent observations and models. *Space Science Reviews*, *184*(1-4), 173–235. https://doi.org/10.1007/s11241-014-0104-0

Kulikov, Y. N., Lammer, H., Lichtenegger, H. I. M., Penz, T., Breuer, D., Spohn, T., et al. (2007). A comparative study of the influence of the active young Sun on the early atmosphere of Earth, Venus, and Mars. *Space Science Reviews*, *129*(1-3), 207–243. https://doi.org/10.1007/s11214-007-9192-4

Li, K., Eriksson, A., André, M., Engwall, E., Wei, Y., Kronberg, E. A., et al. (2012). On the ionospheric source region of cold ion outflow. *Geophysical Research Letters*, *39*, L18102. https://doi.org/10.1029/2012GL053297

Li, K., Haaland, S., Eriksson, A., André, M., Engwall, E., Wei, Y., et al. (2013). Transport of cold ions from the polar ionosphere to the plasma sheet. *Journal of Geophysical Research: Space Physics*, *118*, 5467–5477. https://doi.org/10.1002/jgra.50518

Li, K., Wei, Y., André, M., Eriksson, A., Haaland, S., Kronberg, E. A., et al. (2017). Cold ion outflow modulated by the solar wind energy input and tilt of the geomagnetic dipole. *Journal of Geophysical Research: Space Physics*, *122*, 10,658–10,668. https://doi.org/10.1002/2017JA024642

Lu, G., Richmond, A. D., Lühr, H., & Paxton, L. (2016). High-latitude energy input and its impact on the thermosphere. *Journal of Geophysical Research: Space Physics*, *121*, 7108–7124. https://doi.org/10.1002/2015JA022294

Lundin, R., Lammer, H., & Ribas, I. (2007). Planetary magnetic fields and solar forcing: Implications for atmospheric evolution. *Space Science Reviews*, *129*(1-3), 245–278. https://doi.org/10.1007/s11214-007-9176-4

Lybekk, B., Pedersen, A., Haaland, S., Svenes, K., Fazakerley, A. N., Masson, A., et al. (2012). Solar cycle variations of the Cluster spacecraft potential and its use for electron density estimations. *Journal of Geophysical Research*, *117*, A01217. https://doi.org/10.1029/2011JA016969

Mac-Mahon, R. M., & Gonzalez, W. D. (1997). Energetics during the main phase of geomagnetic superstorms. *Journal of Geophysical Research*, *102*, 14,199–14,207. https://doi.org/10.1029/97JA01151

Maes, L., Maggiolo, R., DeKeyser, J., André, M., Eriksson, A. I., Haaland, S., et al. (2017). Solar illumination control of the polar wind. *Journal of Geophysical Research: Space Physics*, *122*, 468–480. https://doi.org/10.1002/2017JA024615

Milan, S. E. (2009). Both solar wind-magnetosphere coupling and ring current intensity control of the size of the auroral oval. *Geophysical Research Letters*, *36*, L18101. https://doi.org/10.1029/2009GL039997

Moore, T. E., Chappell, C. R., Chandler, M. O., Craven, P. D., Giles, B. L., Pollock, C. J., et al. (1997). High-altitude observations of the polar wind. *Science*, *277*(5324), 349–351. https://doi.org/10.1126/science.277.5324.349

Moore, T. E., & Horwitz, J. L. (2007). Stellar ablation of planetary atmospheres. *Reviews of Geophysics*, *45*, RG3002. https://doi.org/10.1029/2005RG000194

Nilsson, H., Engwall, E., Eriksson, A., Puhl-Quinn, P.-A., & Arvelius, S. (2010). Centrifugal acceleration in the magnetotail lobes. *Annales de Geophysique*, *28*(2), 569–576. https://doi.org/10.5194/angeo-28-569-2010

Olsen, R. C. (1982). The hidden ion population of the magnetosphere. *Journal of Geophysical Research*, *87*, 3481–3488. https://doi.org/10.1029/JA087iA05p03481

Perreault, P., & Akasofu, S.-I. (1978). A study of geomagnetic storms. *Geophysical Journal of the Royal Astronomical Society*, *54*(3), 547–573. https://doi.org/10.1111/j.1365-246X. 1978.tb05494.x

Siscoe, G. L., & Huang, T. S. (1985). Polar cap inflation and deflation. *Journal of Geophysical Research: Space Physics*, *90*, 543–547. https://doi.org/10.1029/JA090iA01p00543

Su, Y.-J., Horwitz, J. L., Moore, T. E., Giles, B. L., Chandler, M. O., Craven, P. D., et al. (1998). POLAR wind survey with the thermal ion dynamics experiment/plasma source instrument suite aboard POLAR. *Journal of Geophysical Research*, *103*, 29,305–29,337. https://doi.org/10.1029/98JA02662

Wei, Y., Pu, Z., Zong, Q., Wan, W., Ren, Z., Fraenz, M., et al. (2014). Oxygen escape from the Earth during geomagnetic reversals: Implications to mass extinction. *Earth and Planetary Science Letters*, *394*, 94–98. https://doi.org/10.1016/j.epsl.2014.03.018

Welling, D. T., André, M., Dandouras, I., Delcourt, D., Fazakerley, A., Fontaine, D., et al. (2015), The Earth: Plasma sources, losses, and transport process). *Space Science Reviews*, *192*(1-4), 145–208. https://doi.org/10.1007/s11214-015-0187-2

Yau, A. W., Takumi, A., & Peterson, W. K. (2007). The polar wind: Recent observations. *Journal of Atmospheric and Solar: Terrestrial Physics*, *69*(16), 1936–1983. https://doi.org/10.1016/j.jastp.2007.08.010